1st Australian MR in Radiotherapy Meeting

Incorporating the Australian MRI LINAC Meeting

December 6-7, 2018

Novotel North Beach

Wollongong, Australia

AUSMRRT.COM Program 2018,
Venue: Novotel North Beach Wollongong
Thursday 6th December

Time	Talk Title	Speaker/Speakers
9.00-9.15	Welcome	Paul Keall, Michael Barton
Session	MRI Linac	Chair: Paul Keall
Keynotes		
9.15-10.00	Plenary Lecture: Adaptation and Tumor Response Assessment with an MR-Linac	Carri Glide-Hurst
10.00-10.30	Invited Talk: Dosimetric optimisation and commissioning status of the Australian MRI-Linac	Urszula Jelen
10.30-11.00	Morning Tea	
Session	MRI Linac Program Grant Research	Chairs: Lois Holloway and William Price
Proffered		
10.30-10-40	Pre-clinical Investigation of Nanoparticle Contrast for Radiosensitisation on the Australian MRI Linac	Hilary Byrne
10.40-1050	Hypoxia-Specific MRI Contrast Agents	Abhishek Gupta
10.50-11.00	Investigations of an EPID Based 3D Dose Reconstruction Method for Applications in MRI-Linac Radiotherapy	Adam McNeilly
11.00-11.10	Diamonds on the Inside: Imaging Nanodiamonds with Hyperpolarized MRI	David Waddington
11.10-11.20	Computer Aided Diagnosis of Prostate Cancer using Non-Contrast Multiparametric MRI	Neda Gholizadeh
11.20-11.30	Broadening the Horizon of Radiotherapy: Atrial Fibrillation Stereotactic Arrhythmic Radioablation (STAR)	Suzanne Lydiard
11.30-11.40	MRI-Compatible Robotics for Quality Assurance in MRI-Linac	Xue Yin Zhang
11.40-11.50	Experimentally Derived Ion Chamber Magnetic Field Correction Factors using a Variable Field on an In-Line MR-Linac	Jarrad Begg
11.50-12.00	Skin Dosimetry of the Australian MRI-Linac	Elizabeth Patterson
12.00-1.00	Lunch	
Session	New Technologies	Chair: Stuart Crozier
Keynote		
1.00-1.30	Invited Talk: SABR for Paediatric patients	Tomas Kron

Proffered		
1.40-1.50	The Design and Performance Analysis of an 8-Element Torso Coil Array for the MRI-Linac System	Mingyan Li
1.50-2.00	Sensitivity Bias Correction of a Surface Coil Array for the MRI-Linac System	Mingyan Li
2.00-2.10	Gradient Nonlinearity (GNL) Correction for MRI-Linac System	Shanshan Shan
2.10-2.20	Real-Time Delivery Verification for MLC Tracking Radiotherapy using Time-Resolved EPID Imaging	Ben Zwan
2.20-2.30	Fully-Automated Bone Segmentation of Multiple Bone Metastases from Lung Primary using FDG-PET/CT Images	Rashmi Nigam
Session	Hot Debate	Chair: Kylie Dundas
2-30-3.00	Proposition: AI Should Replace Radiation Oncologists	For: Michael Barton and Senthilkumar Gandhidasan Against: Tomas Kron and Stuart Crozier
3.00-3.30	Afternoon Tea	
Session	MRI-Linac Dosimetry Research Projects	Chair: Peter Metcalfe
Proffered		
3.30-3.40	Duo Silicon Array Detector Profiles in Transverse and Inline Static Magnetic Fields	Sarah Alnaghy
3.40-3.50	Linac Photon Beam Dosimetry using a Plastic Scintillation Dosimeter and a Convolutional Neural Network	Levi Madden
3.50-4.15	Invited Talk: MRI Guided Protons	Bradley Oborn
4.15-4.30	Opportunities in the Proton Space	Guests
Discussion 4.30-5.00	Introduction of Clinical MRI-Linacs to Australia – Proposal for a Nationally Coordinated Approach. Including Clinical Rationale and Expected Challenges from the Australian Early Adopters	Paul Keall, Carri Glide-Hurst and Carsten Brink

Dinner 6.30 pm Steamers Restaurant, 300 m walk south. Theme Tropical Shirt (optional)

Friday 7th December

Time	Talk Title	Speaker/Speakers
Session	MRI-Linac & Rotating Couch	Chair: Gary Liney
Keynotes		
9.15-9.50	Plenary Lecture: Elekta Unity Linac Experience	Carsten Brink
9.50-10.20	Invited Talk: The Pros, Cons, Implications and Future Exploration Needed in Novel Patient Rotation Systems for Radiation Therapy	Tanya Kairn
10.20-10.30	First Experiences with Healthy Volunteer Rotation for MRI-Guided Radiotherapy: The PAROT Study	Jarryd Buckley
10.30-10.45	Morning Tea	
Session	MRI in treatment Planning-Part 1	Chair Robba Rai
Keynote		
10.45-11.10	Plenary Lecture: Toward High Fidelity MR-Only Treatment Planning	Carri Glide-Hurst
11.10-11.35	Invited Talk: Deformable Registration	Jason Dowling
1135.-12.00	Invited Talk: Clinical Sites for MRI Sim	Lois Holloway
12.00-12.10	Imaging Respiratory Induced Tumour Motion using 4D-MRI for Lung Cancers	Danny Lee
12.10-1.00	Lunch	
Session	MRI in Treatment Planning Part 2	Chair: Dean Cutajar
Keynotes		
1.00-1.30	Invited Talk: MRI Simulation at Liverpool: Update on Clinical Utilisation and R&D	Robba Rai
1-30-2.00 pm	Invited Talk: A multi-centre study for Implementation of MRI-only Prostate Planning	Peter Greer
2.00-2.10	Distortion studies on a 3T MRI: Lung Tumour Susceptibility	Madeline Carr
Session	Panel Discussion	Chair: Michael Barton
2.10-2.50	“Clinical sites best suited to MRI-Linac?”	Peter Metcalfe, Tomas Kron, Lois Holloway
2.50-3-15	Future of MR in RT MRI-Linacs and the Australian MRI-Linac Program	Paul Keall
3.15-3.30	Afternoon Tea	
3.30	Close	

Proffered Papers

PRE-CLINICAL INVESTIGATION OF NANOPARTICLE CONTRAST FOR RADIOSENSITISATION ON THE AUSTRALIAN MRI-LINAC

Hilary Byrne[1], Bin Dong[2], Urzsula Jelen[2], Gary Liney[2], Tara Roberts[2,3], Zdenka Kuncic[1]

[1] The University of Sydney, Sydney, NSW 2006, Australia, hilary.byrne@sydney.edu.au
[2] Ingham Institute for Applied Medical Research, Liverpool, NSW 2170, Australia
[3] School of Medicine, Western Sydney University, NSW 2560, Australia

Introduction: Nanoparticles comprised of a high atomic number material have been shown to enhance dose deposition and tumour control probability of radiotherapy *in vitro* and *in vivo* [1]. This offers the promise of developing a treatment that can extend survival times of patients with poor prognosis cancer.

AGuIX® nanoparticles incorporate gadolinium, which gives bright MR contrast, and has been shown to exhibit radiosensitisation [2,3,4]. The nanoparticles are ideally suited to use on an MRI-linac where the MR image contrast improves definition of the target, while verifiying nanoparticle tumour uptake at time of treatment to confirm radioenhancement.

Materials and Methods: Male Fischer F344 rats were implanted with 9L gliosarcoma cells via stereotaxic surgery at 10 weeks old. The tumour was observed to grow aggressively, with a lifespan of 17-21 days when no treatment is given.

Pilot studies were carried out to establish protocols for pre-clinical animal workflows in the Australian MRI-linac bunker. Rats are anaesthetized with a ketamine/xylazine mixture in the Biological Resources Unit of the Ingham Institute for Applied Medical Research and then transported to the bunker.

For the duration of imaging and the planned radiotherapy treatment rats will remain anaesthetised on a heat pad, placed within a human head coil on the patient treatment bench (see Figure 1). The rat is not restrained, but is closely monitored for movement. During irradiation this is done by cine-MRI, with capture frames every 0.6 s allowing tracking of the rat's breathing and confirming the head has not moved from the treatment set-up position.

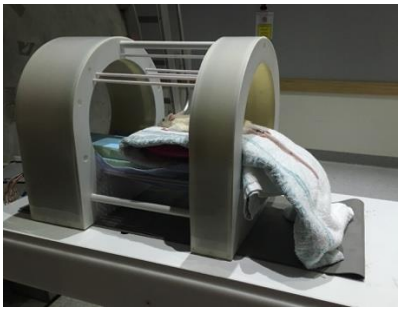

Figure 1. Set-up of rat on heating pad within the head coil on the patient bench of the Australian MRI-linac

Results: The quality of imaging with the head coil is sufficient to identify the rat brain with a T2 anatomical scan, allowing targeting of the radiotherapy beam, verified with a radiation test on a carcass (Figure 2).

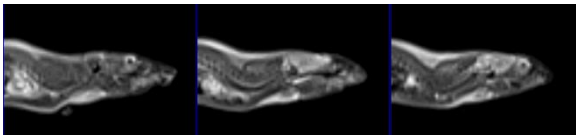

Figure 2. T2-weighted images showing rat brain

After injection of AGuIX nanoparticles, bright enhancement of the tumour at 12 days after implantation was observed (Figure 3). After one hour, approximately 60% of the initial contrast still remained.

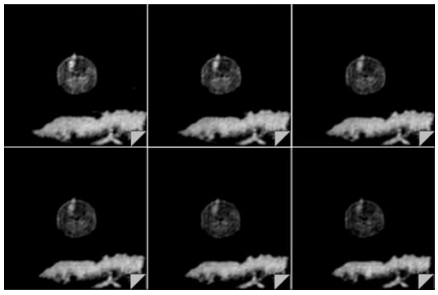

Figure 3. T1-weighted images taken every 10-minutes over 1 hour, showing AGuIX contrast enhancement of the tumour

Cine-MRI image sequences were acquired to observe slight head movements as a rat recovers from anaesthesia.

Conclusions: Pre-clinical pilot studies have been carried out for the first time on the Australian MRI-linac. A custom designed head coil, which allows free passage for the radiotherapy beam, delivers sufficient image quality for whole-brain radiotherapy targeting. AGuIX® nanoparticles have been successfully injected and were found to show a far slower washout from the tumour than standard gadolinium contrast. The groundwork has been laid for the first therapeutic irradiation to be carried out on the Australian MRI-linac in January 2019.

Acknowledgements: The authors gratefully acknowledge support in kind and product information provided by NH TherAguix.

References:

1. Z. Kuncic and S. Lacombe, *Phys. Med. Biol.* **63** 2, 02TR01 (2018)
2. G. Le Duc et al., *ACS Nano* **5**, 9566 (2011)
3. S. Dufort et al., *Sci. Rep.* **6**, (2016)
4. A. Detappe et al., *J. Control. Release* **238**, 103 (2016)

HYPOXIA-SPECIFIC MRI CONTRAST AGENTS

Abhishek Gupta[1*,2], Dj Wijeskera[1,2], Mohammed S. Zaman[3], and William S. Price[1]

[1] Nanoscale Organisation and Dynamics Group, School of Science and Health, Western Sydney University, Penrith, NSW, 2751, abhishek.gupta@westernsydney.edu.au
[2] Ingham Institute of Applied Medical Research, Liverpool, NSW, 2170,
[3] School of Science and Health, Western Sydney University, Penrith, NSW, 2751,

Introduction: Hypoxia or decreased availability of oxygen in tumours is of significant interest in oncology as it is known to increase radiotherapy and chemotherapy resistance, and promote tumour progression [1, 2]. For better prognosis of solid tumours, it is vital to be able to identify and quantify the extent of hypoxia in the different regions of a tumour. MRI provides a non-invasive and safe (i.e., without using any ionising radiation) means of visualising tumours [3, 4]. Paramagnetic contrast agents, often injected intravenously in the patients before an MRI scan, enhance image contrast to assist in the delineation of the tumours [5]. However, as none of the current commercially available MRI contrast agents is hypoxia-specific, it is difficult to visualise hypoxic regions of tumour directly using contrast enhanced MRI.

This presentation reports on the development and characterisation of a nanoparticle-based MRI contrast agent system with the ability to actively target hypoxic cells.

Materials and Methods: 2-nitroimidazole, which is known to target hypoxic cells, was incorporated within the bilayer membranes of liposomal nanoparticles, along with commercially available paramagnetic lipids (to impart MRI contrast). In-vitro contrast enhancement efficiency of the liposomes was characterised using NMR relaxation and chemical shift measurements [6]. Their hypoxia-targeting ability was assessed in two cell lines: SH-SY5Y human neuroblastoma and MCF-7 human breast cancer cell lines. Each cell line was seeded in three different tissue culture flasks. One flask was made hypoxic by continuously passing N_2 through it and the other two were kept normoxic (with a constant flow of air). After treating each flask with the same amount of liposomes for 2 hours, the cells were imaged using MRI, and then digested in nitric acid for inductively coupled plasma – mass spectrometry (ICP-MS) analysis.

Results: Paramagnetic liposomes with and without 2-nitroimidazole lipids were successfully formulated, with an average diameter of 100 nm. Cellular uptake experiments in hypoxic and normoxic conditions displayed a distinct preference of the liposomes with 2-nitroimidazole towards hypoxic cells. The ICP-MS results, in particular, revealed that there was up to five times higher accumulation of gadolinium in hypoxic cells compared to the normoxic cells. This effect was exclusive to the liposomes containing 2-nitroimidazole and was not observed for non-targeted liposomes.

MRI (at 14.1 T), on the other hand, did not show any significant contrast difference between hypoxic and normoxic cells. Upon further investigation, this was found to be due to the low gadolinium concentrations used in the cellular uptake experiments, and low contrast enhancement efficiencies observed at 14.1 T.

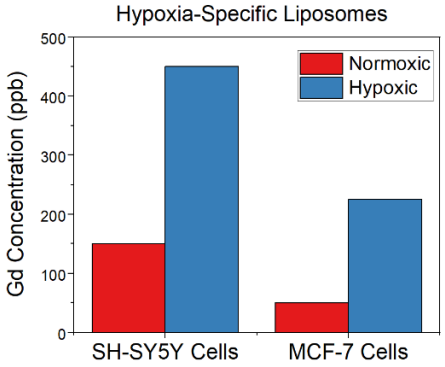

Figure 1. Gd concentrations measured by ICP-MS in hypoxic and normoxic cells. Up to five times higher Gd accumulation in hypoxic cells confirms the hypoxia-specificity of the liposomes.

Conclusions: Hypoxia-specific paramagnetic liposomes have been succesfully developed. With the well-known drug/radiosensitizer delivery capability of liposomes, this study brings us a step closer towards the development of hypoxia-targeting 'MRI-Linac' prodrugs.

Acknowledgements: The authors acknowledge the support of the Australian National Health and Medical Research Council Program Grant APP1132471. The facilities and the scientific and technical assistance of the National Imaging Facility, Western Sydney University Node is also gratefully acknowledged.

References:

1. M. C. Brahimi-Horn et al., *J. Mol. Med.* **85**, 1301-1307 (2007).
2. A. M. Shannon et al., *Cancer Treat. Rev.* **29**, 297-307 (2003).
3. A. P. Pathak et al., In *Methods in Enzymology*, **386**, Academic Press, 1-58 (2004).
4. A. Gupta et al., In *Theory Dynamics and Applications of Magnetic Resonance Imaging - I*, Science Publishing Group, 3-33 (2014).

INVESTIGATIONS OF AN EPID BASED 3D DOSE RECONSTRUCTION METHOD FOR APPLICATIONS IN MRI-LINAC RADIOTHERAPY

Adam McNeilly[1], Peter Greer[1,2], Timothy Van Beek[3], Eric Van Uytven[3], Todsaporn Fuangrod[4], Krista Chytyk-Praznik[5], Benjamin Zwan[6]

[1] School of Mathematical and Physical Sciences, University of Newcastle, Callaghan, NSW, Australia (adam.mcneilly@uon.edu.au)
[2] Department of Radiation Oncology, Calvary Mater Newcastle Hospital, Waratah, NSW, Australia
[3] Medical Physics Department, CancerCare Manitoba, Winnipeg, Manitoba, Canada
[4] Faculty of Medicine and Public Health, HRH Princess Chulabhorn College of Medical Science, Chulabhorn Royal Academy, Bangkok, Thailand
[5] Medical Physics Department, Nova Scotia Cancer Centre, Halifax, Nova Scotia, Canada
[6] Central Coast Cancer Centre, Gosford Hospital, Gosford, NSW, Australia

Introduction: One of the challenges of external beam radiotherapy (EBRT) with conventional linacs is that tumours tend to move both between treatment fractions (interfraction motion) and during the treatment itself (intrafraction motion). The MRI-Linac could provide real-time tracking of tumours and better adaptive treatment planning accounting for both intrafraction and interfraction patient motion[1]. We aim to adapt a predictive fluence model and use this with images from an Electronic Portal Imaging Device (EPID) to reconstruct dose delivered to the patient on the Australian MRI-Linac system.

Methods: We utilize a fluence model that predicts the EPID dose[2,3], as well as a patient dose reconstruction (PDR) algorithm[4] that back-projects this dose to the patient plane and calculates the three-dimensional patient dose via a collapsed cone convolution method.

We will adapt the model and algorithm to calculate the patient dose for the Australian MRI-Linac system, accounting for the various differences including the magnetic field of the MRI, larger SAD and SDDs, and the horizontal linac beam orientation.

Results: The PDR algorithm has been demonstrated to work on a conventional TrueBeam linac using some simple square field plans as well as two clinical IMRT plans.

A preliminary model for the Australian MRI-Linac has been made and is in the process of being optimized and tested. The model currently predicts the correct central axis values and FWHMs of the EPID dose profiles, but agreement at the field edges and penumbra still needs improvement (see Figure 1).

Conclusions: MRI guided radiotherapy has the potential to greatly improve image guided radiotherapy for cancer patients. Once our prediction model is completed we will be able to reconstruct and verify the accuracy of the dose delivered to patients during treatments on the Australian MRI-Linac system.

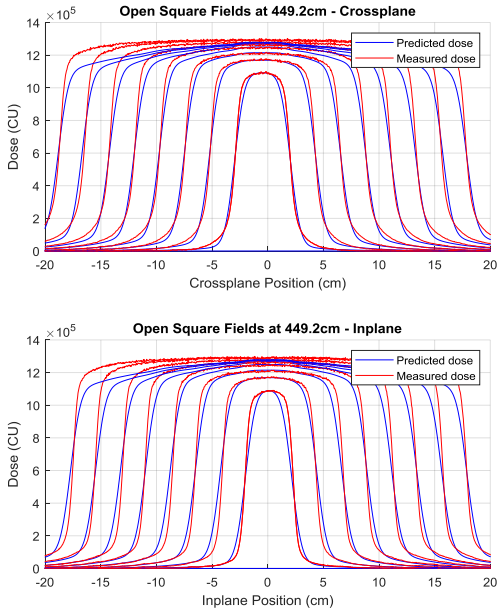

Figure 1. The predicted EPID dose vs measured EPID dose for multiple field sizes on the Australian MRI-Linac.

References:

1. The Australian Magnetic Resonance Imaging-Linac Program (P.J. Keall et al), *Sem. Rad. Onc.* **24**, 203-206 (2014).
2. Comprehensive fluence model for absolute portal dose image prediction (K. Chytyk et al), *Med. Phys.* **36**, 1389-1398 (2009).
3. Model-based prediction of portal dose images during patient treatment (K. Chytyk-Praznik et al), *Med. Phys.* **40**, 031713 (11pp.) (2013).
4. Validation of a method for in vivo 3D dose reconstruction for IMRT and VMAT treatments using on-treatment EPID images and a model-based forward-calculation algorithm (E. Van Uytven et al), *Med. Phys.* **42**, 6945-6954 (2016).

DIAMONDS ON THE INSIDE:
IMAGING NANODIAMONDS WITH HYPERPOLARIZED MRI

David E. J. Waddington[1,2]
[1]School of Physics, The University of Sydney, NSW, Australia
[2]A. A. Martinos Center for Biomedical Imaging, Massachusetts General Hospital, Charlestown, MA, USA
david.waddington@sydney.edu.au

Introduction: Nontoxic nanodiamonds (NDs) have proven useful as a vector for therapeutic drug delivery to cancers[1] and as optical bioprobes of subcellular processes.[2] Despite their potential clinical relevance, an effective means of noninvasively imaging NDs *in vivo* is still lacking. This presentation explores how intrinsic paramagnetic defects in ND can be used to hyperpolarize nuclei via microwave-based dynamic nuclear polarization (DNP) techniques. Subsequently, I outline new modalities developed collaboratively during my PhD that enable direct imaging of NDs via hyperpolarized ^{13}C MRI[3,4] and indirect imaging of NDs via Overhauser-enhanced MRI (OMRI).[5]

Materials and Methods: Synthetic NDs were selected after electron paramagnetic resonance (EPR) analysis verifying the presence of appropriate spin-1/2 paramagnetic defects for hyperpolarization.

For ^{13}C imaging shown in Fig. 1, the 1.1% abundant ^{13}C nuclear spins in ND are first hyperpolarized via microwave irradiation at 3 T and 5 K in a home-built DNP system, yielding ^{13}C polarizations up to 24,000 times larger than Boltzmann polarization at room temperature.[5] Anatomical (^{1}H) and ND imaging (^{13}C) is performed after subsequent dissolution and transfer of NDs to a 7 T MRI scanner.

Overhauser-imaging in Fig. 2 was performed at 6.5 mT in an ultra-low field (ULF) MRI scanner[6] using an efficient balanced steady-state free precession (b-SSFP) OMRI sequence at room temperature. A homebuilt DNP probe was constructed (Electron frequency: 191 Mhz and ^{1}H frequency: 276 kHz) to image 125 nm NDs in water solution.

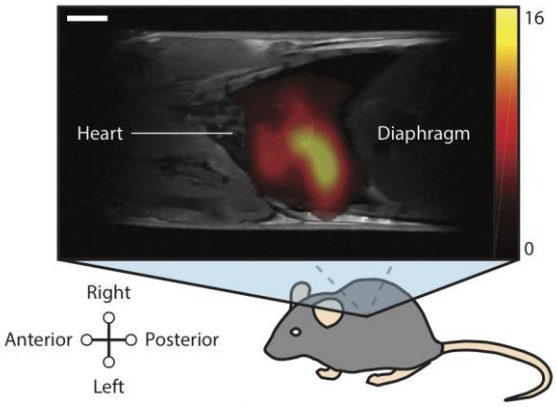

Figure 1. Co-registered ^{1}H:^{13}C MRI of a mouse following *post-mortem*, intrathoracic injection of hyperpolarized 2 μm diamond particles. Grayscale shows mouse anatomy. Colorbar shows the ^{13}C signal that results from the presence of hyperpolarized NDs. White scale bar is 3 mm in length.

Results: Background-free ^{13}C imaging of hyperpolarized NDs in a mouse thorax is demonstrated in Fig. 1. The extremely-long T_1-relaxation times of ^{13}C nuclei in ND enable ^{13}C imaging over timescales as long as 30 minutes after hyperpolarization.

Conventional ^{1}H ULF MRI of ND solution is shown in Fig. 2(b). OMRI acquisition includes a saturation pulse at the electron frequency. This pulse drives spin polarization from defects at the ND surface to ^{1}H nuclei in solution via the Overhauser effect, modulating the ^{1}H MRI signal and clearly showing the location of NDs in solution (see Fig. 2(c,d)). The *in-situ* hyperpolarization mechanism allows ND contrast to be switched 'on' or 'off' over indefinitely long periods of time.

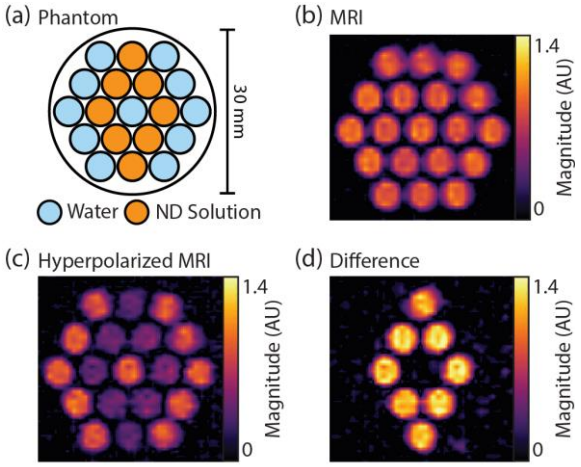

Figure 2. Images of a ND phantom acquired at 6.5 mT. (a) Phantom schematic. (b) Standard ^{1}H b-SSFP MRI acquisition. (c) ^{1}H b-SSFP OMRI acquisition. The ^{1}H-e^{-} coupling generates contrast in the 125 nm ND solution. (d) Difference of b/c.

Conclusion: New modalities for noninvasively imaging ND have been developed. ND has been established as a biocompatible platform for drug delivery and hence, these results promise new *in vivo* applications of hyperpolarized MRI in the field of nanotheranostics.

References:

1. E. K. Chow et al., *Sci. Trans. Med.*, **73**, 73ra21 (2011).
2. L. P. McGuinness et al., *Nature Nano*, **6**, 358-63 (2011).
3. D.E.J. Waddington et al, *arXiv*, 1709.0185 (2017).
4. E. Rej et al, *Nat. Commun.*, **6**, 9459 (2015).
5. D.E.J. Waddington et al., *Nat. Commun.*, **8**, 15118 (2017).
6. M. Sarracanie et al., *Sci. Rep.*, **5**, 15177 (2015).

COMPUTER AIDED DIAGNOSIS OF PROSTATE CANCER USING NON-CONTRAST MULTIPARAMETRIC MRI

N. Gholizadeh[1](neda.gholizadeh@uon.edu.au), P. B. Greer[2,3], J. Simpson[2,3], P. Lau[4,5], S. Ramadan[1,5]
[1]School of Health Sciences, Faculty of Health and Medicine, University of Newcastle, NSW 2308, Australia
[2]Calvary Mater Newcastle, Radiation Oncology department, Newcastle, NSW, Australia.
[3]University of Newcastle, School of Mathematical and Physical Sciences, NSW, Australia
[4]Calvary Mater Newcastle, Radiology department, Newcastle, NSW, Australia.
[5]Hunter Medical Research Institute (HMRI) Imaging Centre, New Lambton Heights, NSW, Australia

Introduction: At present, the ability of non-invasive identification of prostate cancer (PCa) for diagnosis remains challenging. Clinical application of magnetic resonance images (MRI) has been shown to improve the detection of prostate cancer. In addition, multi-parametric MRI (mp-MRI), which combines T2-weighted imaging (T2WI), with methods including diffusion-weighted imaging (DWI) and dynamic contrast enhancement (DCE) are utilized clinical management of prostate cancer. Mp-MRI using T2WI and diffusion tensor imaging (DTI) and magnetic resonance imaging (MRSI) are not currently used for prostate cancer diagnosis. Difficulties in the processing and interpretation of MRSI/DTI has limited the role of these imaging in the clinic. However, Prostate DTI and MRSI have undergone several technical improvements and shows promises for prostate tumour detection and localization [1,2]. In this study, the role of mp-MRI, including T2WI, DWI, DTI and MRSI investigated for peripheral zone prostate cancer assessment.

Materials and methods: 12 PCa patients (71.16 ± 8.17 years) were analysed. Ethics approval for the study was obtained and written informed consent was obtained from all patients. Participants were scanned using a 3 tesla MRI scanner (Skyra, Siemens Healthineers, Germany) equipped with an phase array coil. T2WI was obtained using a two-dimensional turbo spin echo (TSE). DWI was obtained using single shot echo planar imaging (EPI) and b-values of 0, 400 and 800 s/mm^2. DTI was also obtained using a single shot EPI. 3D 1H MRSI data was acquired using a GOIA-sLASER sequence with a voxel size of 7×7×7 mm^3.

A total of 41 cancer region of interests (ROI)s were manually outlined in the peripheral zone (PZ) on T2WI by a radiologist. A two tailed t-test was used to compare the mean values of cancer and healthy regions using IBM SPSS statistic version 0.24.0 software. The area under receiver operating characteristic (ROC) curves of different combinations of MRI sequence were measured to evaluate the performance of mp-MRI for discriminating cancer and non-cancer regions.

Results: Mean ADC values of DWI and mean diffusivity (MD) values of DTI in healthy regions were significantly higher than cancer regions (p-value < 0.01), whereas mean fractional anisotropy (FA) values of DTI in healthy regions was significantly lower than cancer regions (p-value < 0.01).

For MRSI, the concentration of choline (Cho), creatine (Cr), polyamine (PA) and citrate (Cit) were measured using LCmodel and the ratio of Cho+Cr+PA/Cit and Cho/Cit were calculated. The mean Cho+Cr+PA/Cit and Cho/Cit ratios in the cancer regions was significantly higher than the healthy regions (p-value < 0.05). T2WI+DWI+DTI+MRSI increased the diagnostic performance with an area under the ROC curve of 0.991 and (Figure 1). The sensitivity and specifity of different combinations of MRI sequence were summarized in Table 1.

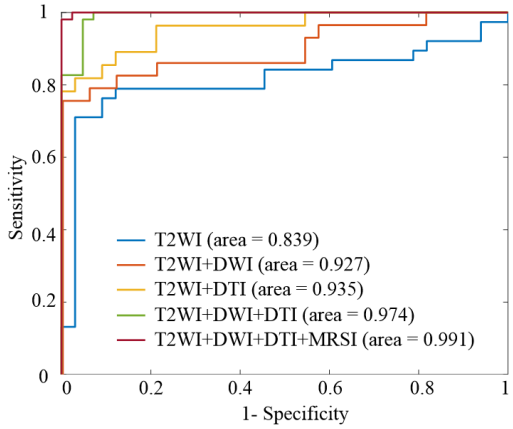

Figure 1. ROC curve of different combinations of MRI sequence for cancer vs healthy regions

Table 1. Sensitivity and specificty of different combination of MRI sequence for cancer vs healthy regions

MRI Sequence	Sensitivity	Specificity
T2WI	0.918	0.705
T2WI+DWI	0.938	0.902
T2W +DTI	0.957	0.917
T2WI+DWI+DTI	0.982	0.937
T2WI+DWI+DTI+MRSI	1.00	0.964

Conclusion: Our results suggest that mp-MRI using DWI, DTI and MRSI in combination with structural T2WI improve performance for discrimination of cancer and healthy prostate tissues.

References:

1. Innovative diffusion MRI protocol to improve prostate cancer diagnosis (C. Shenhar et al.), Eur Uro Supplements e1883-e1884 (2017).

2. Improved volume selective (1) H MR spectroscopic imaging of the prostate with gradient offset independent adiabaticity pulses at 3 tesla (I.K Steinseifer et al.), Magn Reson Med 74(4):915-24 (2015).

BROADENING THE HORIZON OF RADIOTHERAPY: ATRIAL FIBRILLATION STEREOTACTIC ARRHYTHMIC RADIOABLATION (STAR)

Suzanne Lydiard[1,2], Beau Pontre[3], Boris Lowe[2], Paul Keall[1]

[1] ACRF Image X Institute, University of Sydney, Sydney, Australia. Email: slydiard@adhb.govt.nz
[2] Auckland City Hospital, Auckland, NZ
[3] Centre for Advanced MRI, University of Auckland, Auckland, NZ

Introduction: The prevalence and socioeconomic burden of Atrial Fibrillation (AF) is rapidly increasing due to aging population and current treatment limitations. Stereotactic arrhythmic radioablation (STAR) is a potential non-invasive treatment alternative. However, AF STAR has challenges; it requires high radiation doses, target motion is a superposition of respiratory motion and cardiac contraction, and AF patients' long life-expectancies means radiation risks must be minimized. We hypothesise MRI-Linacs will provide the safest AF STAR delivery due to their non-invasive real-time targeting and treatment adaptation capabilities. The purpose of this work is to investigate the feasibility of real-time MRI AF STAR targeting. This includes MRI sequence optimisation for target volume (TV) visualisation, quantifying anatomical motion, and developing a real-time target tracking method.

Methods: In an initial Pilot study, four healthy volunteers underwent non-contrast cardiac MRI on a Magnetom Skyra 3T scanner (Siemens, Germany). Many sequences were trialled and optimised for target visualisation, including cardiac-gated and respiratory navigated 3D sequences, breath-hold (BH) cardiac gated 2D cine sequences, and fast free-breathing (FB) acquisition 2D cine. Image quality and target visualisation were qualitatively assessed and discussed by the research team including a Cardiologist, Radiation Oncologist, and MRI Physicist.

To study TV motion, 2D FLASH BH cine stacks were acquired in three healthy volunteers. 8-16 slices were acquired in each of the three magnet orthogonal planes with slice thickness 5mm, 0mm slice gap, 25 frames, TE=2.65ms, TR=21.9-27.6ms, α=10°, 1.44mm^2-1.63mm^2 pixel. This dataset was contoured to provide 3D contours for each cardiac phase. 2D FB single slice cines were also acquired using real-time (RT) TrueFISP for a duration of approximately 10 breaths with slice thickness 5-6mm, TE=2.5-2.61ms, and 200-250ms temporal resolution.

Contouring and motion analysis was performed in MIM Maestro (MIM Software Inc, USA). The TV encompassed myocardium and pulmonary vein transmural at both the left and right pulmonary vein antra. Mean position shifts of 3D or 2D contour centroids throughout the cardiac cycle (diastole-systole) and respiratory cycle (inhalation-exhalation) were recorded.

Results: 3D sequences had insufficient target contrast for delineation, as illustrated in Figure 1. 2D BH FLASH cines provided superior target contrast and image quality than 2D BH TrueFISP cines. RT TrueFISP FB cines had a degradation of image quality, but will provide usable information for real-time target localization.

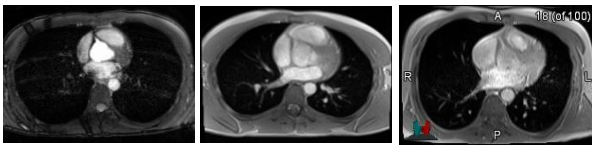

Figure 1. Exemplar images to compare image quality and target visualisation between 3D (left) 2D cine FLASH BH (centre) and 2D RT TrueFISP FB (right). Note: these are acquired from different volunteers.

Preliminary analysis of three volunteers shows TV displacement caused by cardiac contraction (3±1mm anterior-posterior, 2±1mm left-right, 3±1mm superior-inferior) is of similar magnitude to atria displacement (3±2mm anterior-posterior, 3±1mm left-right, 4±1mm superior-inferior). However, the atria and TV's do not necessarily follow the same motion trajectory and the displacement between the centroid of structures is variable throughout the cardiac cycle. Preliminary analysis on single slice RT FB TrueFISP on two volunteers suggests TV and atria displacement with respiration is also of similar magnitude (0.4mm/0.5mm anterior-posterior, 0.3/0.4mm left-right, 11/11mm superior-inferior for TV and atria respectively).

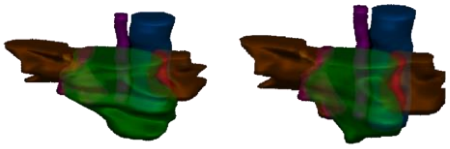

Figure 2. Exemplar 3D contours derived from 2D FLASH cine stacks showing atria (green), pulmonary vein branches (orange), aorta (blue), oesophagus (pink) and approximate target volume (red) when in cardiac systole (left) and diastole (right).

Conclusion: Target visualisation is feasible on non-contrast MRI. Preliminary findings suggest TV and atria displacement throughout the cardiac and respiratory cycle are of comparable magnitude, however the displacement between these structures is not always constant throughout the cardiac cycle. Further data collection and analysis is currently underway to investigate the motion of these structures and develop MR target tracking. Preliminary findings are encouraging for MR-guided MRI-Linac treatment deliveries.

MRI-COMPATIBLE ROBOTICS FOR QUALITY ASSURANCE IN MRI-LINAC

Xue Yin Zhang[1,†], Aidan McDaid[2], Graham Brooker[1,3], Bin Dong[4], Paul Keall[5] and Andre Kyme[1]

[1] Biomedical Engineering, Faculty of Engineering & IT, University of Sydney, Sydney, Australia
[2] Boston University, Boston, USA
[3] Australian Centre for Field Robotics, University of Sydney, Sydney, Australia
[4] Ingham Institute, Liverpool Hospital, Sydney, Australia
[5] ACRF Image X Institute, University of Sydney, Sydney, Australia
† xzha2203@uni.sydney.edu.au

Introduction: Robotic platforms and manipulators can execute highly accurate and reproducible motion, a critical requirement for quality assurance (QA) of motion-adaptive radiotherapy. However, there are currently no robotic systems suitable for MRI-Linac – that is, able to manipulate a 1-2 kg phantom according to rapid multi-axis tumour motion within a high magnetic field. This paper presents an investigation of potential MR-compatible actuation methods and the feasibility of developing an MR-compatible robotic platform for MRI-Linac QA.

Materials and Methods: We tested the impact of four different actuators on the signal-to-noise ratio (SNR) of a uniform water-filled phantom. The actuators were: (i) an ultrasonic ceramic motor (HR1, Nanomotion), (ii) a custom pneumatic air motor (Deprag), (iii) a pneumatic plunger based on an MR-compatible cylinder (Airpel, Airpot), and (iv) our own 3D-printed pneumatic rotary stepper motor. Each actuator was tested stationary/moving in a 1 T MRI-Linac and also in a high-field 7T system (MRS-7000, MR Solutions). SNR was measured using the dual acquisition method [1] (SE, slice 5 mm, TR 1000 ms, TE 30ms).

Based on the SNR analysis we further developed the pneumatic stepper motor concept based on [2]. We adapted this design to incorporate a curvilinear track which could support multiple pneumatic 'carriages' operating in synchrony. The performance of the new stepper design was characterised in terms of its maximum stepping frequency and load capacity.

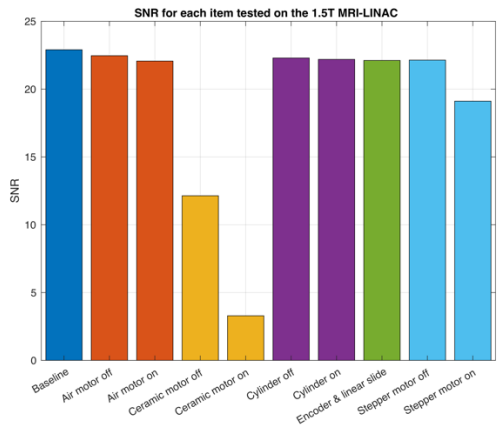

Figure 1. SNR for the water phantom for each actuator (stationary (off) and moving (on)). Also shown is the impact on SNR for two passive components (optical encoder, linear slide), both ostensibly MR-compatible according to manufacturer specifications.

Results: For the 1 T field, the ultrasonic ceramic motor caused moderate (50%) SNR loss when stationary and severe (~85%) SNR loss when moving (Figure 1). By comparison, pneumatic actuation caused no appreciable SNR reduction in either the stationary or moving state. Our results are consistent with previous reports for ultrasonic and pneumatic actuators. SNR results for the 7 T field (not shown) were very similar to 1 T. We also verified that the passive components are indeed truly MR-compatible.

The curvilinear pneumatic stepper motor is shown in Figure 2. Four inlets are sequentially pressurised via two 5/2 solenoid valves switched from a microcontroller to drive four toothed pistons against the track. A sinusoidal tooth profile was used to reduce friction. The motor had a maximum stepping frequency of 37 Hz for pressure >213 kPa. The maximum (tangential) drive load was 1.6 N.

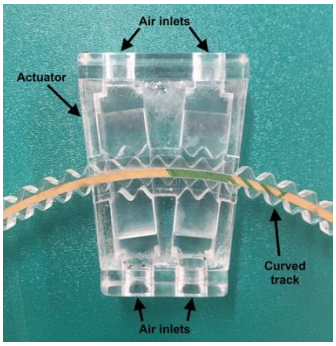

Figure 2. Pneumatic curvilinear stepper motor

Conclusions: Pneumatically-driven actuators are highly amenable to the MR environment. Our pneumatic curvilinear stepper motor design is a novel single-axis actuator capable of reaching high stepping frequencies and a moderate load capacity. Our results suggest that it has good potential for upscaling into a multi-axis robotic platform for MRI. We are currently exploring a multi-actuator, multi-axis design based on [3].

References:

1. A comparison of two methods for measuring the signal to noise ratio on MR images (M.J. Firbank et al.) *Phys. Med. Biol.* **44** N261-64 (1999).
2. Design and characterization of Stormram 4 (V. Groenhuis et al.), *IEEE/RSJ Int. Conf. Intelligent Robot. Syst.* 928-933 (2017).
3. (No name, date) https://www.youtube.com/watch?v=RR4pmNEWuo4&t=307s

Experimentally derived ion chamber magnetic field correction factors using a variable field on an in-line MR-linac

Jarrad Begg[1,2,3] *, Urszula Jelen[1,2], Brendan Whelan[2,4], Bin Dong[1,2], Natalia Roberts[5], Gary Liney[1,2,3,5], Lois Holloway[1,2,3,4,5,6]

1. Department of Medical Physics, Liverpool and Macarthur Cancer Therapy Centre, Sydney, Australia
2. Ingham Institute for Applied Medical Research, Sydney, Australia
3. South Western Sydney Clinical School, School of Medicine, Uni of New South Wales, Sydney, Australia
4. Radiation Physics Lab, University of Sydney, Sydney, Australia
5. Centre for Medical Radiation Physics, Uni of Wollongong, Wollongong, Australia
6. Institute of Medical Physics, School of Physics, Uni of Sydney, Sydney, Australia

Introduction: Reference dosimetry is a requirement for any clinical machine. Ion chamber response changes in magnetic fields, which must be corrected for on MRI-Linacs[1]. Magnetic field correction factors (k_B) have previously been derived from Monte-Carlo simulations[2] or chemical dosimeters[3]. This work presents a methodology for experimentally deriving k_B for an in-line MR-linac.

Materials and Methods: The Australian MR-Linac utilises a unique rail system, allowing movement of chambers into different magnetic field strengths whilst maintaining a constant source to chamber distance[4] and consistent scattering conditions. k_B can be calculated from the ratio of absorbed dose to water at the magnetic field strength relative to absorbed dose at 0 T[5]. Dose deposition to water at depth and beam quality has previously been shown to be independent of the magnetic field[6], therefore k_B can be calculated from the ratio of the output at 0 T relative to the output in the magnetic field. Output for a Farmer chamber was measured at various magnetic field strengths along the MR bore. Output at 0 T was linearly extrapolated and used to calculate k_B. Constancy of the linac's output was measured via two methods; a second chamber between the source and MLC and a diamond detector behind the chamber being investigated.

Results: Figure 1 shows k_B at various magnetic field strengths, with the farmer chamber as reference. k_B at 1 T was 0.987±0.002. A k_B of 0.993±0.002 at 1 T was measured using the diamond detector as a reference. The presented methodology was able to determine k_B similar to chemical dosimetry[3] and Monte-Carlo simulations[2].

Conclusions: Ion chamber magnetic field correction factors (k_B) were derived using a variable magnetic field, demonstrating an approach for determining these factors without Monte-Carlo simulations or chemical dosimeters.

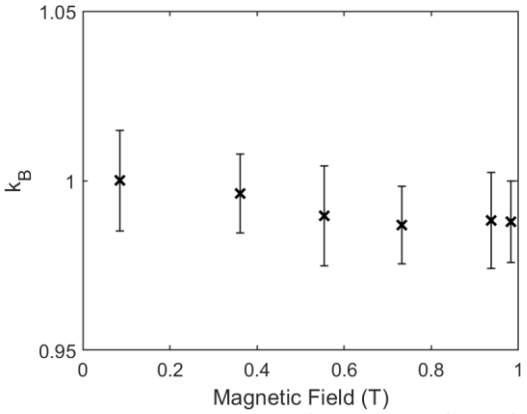

Figure 1. *Measured magnetic field correction factors for the Australian MR-Linac*

References:

1. Dosimetry for the MRI accelerator: the impact of a magnetic field on the response of a Farmer NE2571 ionization chamber. (Meijsing, I., et al), *Phys in Med and Bio*, 2009. **54**(10): p. 2993.
2. Dose response of selected ion chambers in applied homogeneous transverse and longitudinal magnetic fields. (Reynolds, M, et al), *Med Phys*, 2013. **40**(4):
3. Reference dosimetry measurements in the Australian MRI-linac. (Billas, I., et al) in *World Congress on Medical Physics and Biomedical Engineering*. 2018. Prague, Czech Republic.
4. Experimental results from a prototype high-field inline MRI-linac. (Liney, G.P., et al.), *Med Phys*, 2016. **43**(9): p. 5188-5194.
5. Reference dosimetry in magnetic fields: formalism and ionization chamber correction factors. (O'Brien D, et al.) *Medical Physics.* 2016;43(8):4915-4927.
6. Electron contamination modeling and skin dose in 6 MV longitudinal field MRIgRT: Impact of the MRI and MRI fringe field. (Oborn B, et al.), *Med Phys.* 2012;39(2):874-890.

SKIN DOSIMETRY OF THE AUSTRALIAN MRI-LINAC

E Patterson[1,2], N. Roberts[1,2], U. Jelen[2,] D. Cutajar[,1] B.Oborn[1], P. Metcalfe[,1,2]

[1] Centre of Medical Radiation Physics, University of Wollongong, Australia.
[2] Ingham Institute for Applied Medical Research, Liverpool, Australia.

Introduction: The magnetic field of an MRI linac causes pertubations to secondary electron paths due to the Lorentz force. For some inline designs, the fringe field of the magnet results in electrons being focused down the central axis, this introduces unique challenges for radiotherapy dosimetry, particularly at the entry surface (skin) region due to a high dose gradient[1]. The combination of the high dose gradient and the strong magnetic field means commonly used dosimeters, such as an ionization chamber, which are not MRI compatible renders them useless for Australian MRI-linac measurements.

Materials and Methods: Skin dosimetry measurements were obtained using a combination of three dosimeters: MO*Skin* (MOSFET); microDiamond detector and EBT3 Gafchromic™ film. The Australian MRI-linac which has a unique design where the linac is mounted on a rail system allowing for measurements to be performed at different magnetic field strengths while maintaining a constant SSD. The two locations were chosen such that for the first the magnetic field strength was 1 T and the second at ~0 T. PDDs were acquired for a range of field sizes for both locations. For each detector used, the effective point of measurements varies. The MO*Skin* has the ability to provide a depth of measurements of 0.07mm, giving a skin dose equivalent depth when placed on a surface during radiation therapy[2]. In conjunction with the MO*Skin*, a microdiamond detector was used which has an effective depth of measurement of 1mm[3]. The combination of the two detectors along with Gafchromic film enabled a comphrensive PDD to be obtained for each location and field size.

Results: PDDs for a 11.8×11.5cm^2 field are shown in Figure 1 where 1T MO*Skin* data recorded a surface measurement of 385%, relative to D_{max} at 0T. For the fringe field, ~0T location, the surface measurement recorded for the MO*Skin* was 70%. As expected there exists little variation in the 0T data sets for each detector while greater flucations can be seen for the 1T data sets. This can be attributed to the nature of the electron hot spot which exhibits a high dose gradient drop off; hence placement of the detectors sensitive volume can unavoidably vary slightly. At ~20mm depth, electron contamination has been absorbed and the data sets of different set ups correlate well with minimal variance at greater depths.

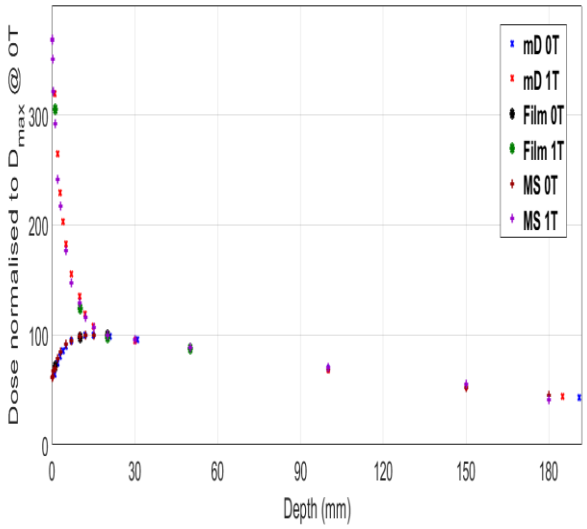

Figure 1. PDD's of 6.1×5.8 cm^2 field using the MOSkin (MO); microdiamond detector (MD) and Gafchromic film (Film).

Conclusion: The MO*Skin* surface dose recorded at 0.07mm was upwards of 385%, relative to Dmax of the 0T location for the 11.8×11.5cm^2 field size. Other fields sizes used also showed considerable surface measurements where for a 23.5×23cm^2 field a dose upwards of 800% was recorded. Now that the surface dose has been characterised for a variety of field sizes, methods to reduce the airbourne electrons will be investigated. Proposed ideas include magnetic purging beyond the MRI fringe field region and with the use of acrylic spoilers placed up stream from the surface.

Acknowledgements:
This work has been funded by the Australian Federal Government's Research Training Program (RTP) and Ingham Institute PhD Top Up Scholarship.

References:

1.Electron contamination modeling and reduction in a 1 T open bore inline MRI-linac system (Oborn, B et al.), *Medical Physics*, 41(5), p.051708 (2014).
2. Review of four novel dosimeters developed for use in radiotherapy (Metcalfe, P et al.) *Journal of Physics: Conference Series*, 444, p.012008 (2013).
3.Microdiamond Synthetic Diamond Detector (PTW), *Product Specifications* (2014).

THE DESIGN AND PERFORMANCE ANALYSIS OF AN 8-ELEMENT TORSO COIL ARRAY FOR THE MRI-LINAC SYSTEM

Mingyan Li[1], Ewald Weber[1], Aurelien Destruel[1], Feng Liu[1], Stuart Crozier[1]
[1] School of Information Technology and Electrical Enginnering, The University of Queensland

Introduction:
The current MRI-LINAC system is equipped with a dedicated transceive RF body coil which is completely radio-transparent and has a uniform field distribution over the diameter of spherical volume (DSV) [1]. In this work, an 8-element RF surface coil array was designed to improve SNR and enable fast MR (parallel) imaging, while maintaining the radio-transparency of the setup. The proposed coil array was designed and evaluated with simulations.

Materials and Methods: As shown in Fig. 1(a), the patient in this MRI-LINAC setup is in supine position and perpendicular to the B_0 field. The proposed 8-element coil array consists of four anterior and four posterior elements (Fig. 1(b)), creating a window for radiation beams on both sides of the patient. As shown in Fig.1(c), the coil array is designed to cover a DSV of 30 cm and the size of the radiation beam window is adjustable from 25 cm to 30 cm. The anterior coil elements were designed to be embedded into a flexible polyester pad, giving flexibility to the opening window and allowing close-fitting of the RF coil to the patient. The length and width of the rectangular coil element is 300 mm (along z direction) and 70 mm, respectively (Fig.1d). The proposed coil array was simulated in FEKO (Altair Engineering, Michigan, US) loaded with a torso phantom with electric properties similar to human muscle (ε_r = 60 and σ = 0.5) The SNR was calculated according to the formula in [1] as:

$$SNR = V_{signal} / V_{noise} \propto B_0^2 \sin(\alpha \,|\, B_1^+ \,|)\,|\, B_1^- \,| / \sqrt{P_{sample}}$$

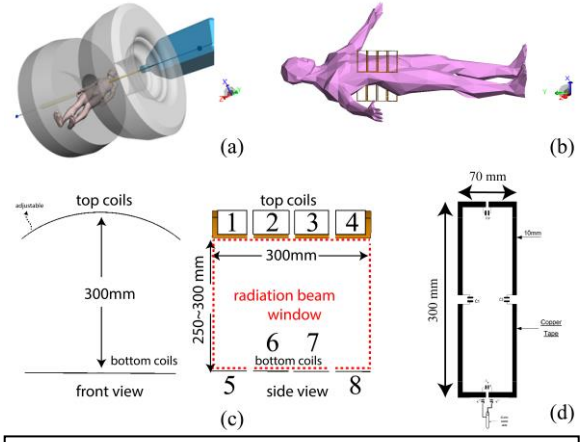

Figure 1 (a) Patient orientation in the MRI-LINAC (supine position and perpendicular to the B_0 field); (b) the proposed 8-element array with a human model; (c) front and side view of the proposed coil array; (d) geometry of an individual coil element.

With the same sequences (like standard gradient echo or spin echo), transmission power (8 W in this work) and transmit profile, the SNR is only dependent on the receive sensitivity (B_1^-) as:

$$SNR_{array} / SNR_{birdcage} = |\, B_1^- \,|_{array} / |\, B_1^- \,|_{birdcage}$$

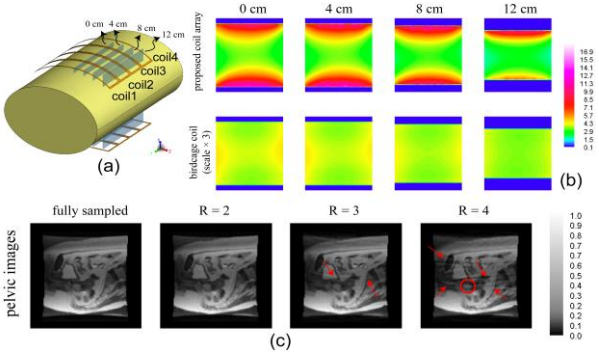

Figure 2 (a) Four slice locations for SNR comparison. (b) SNR maps of two coils at four slice locations. (c) pelvic images when reduction factor was from 1 to 4. Red arrows indicates the aliasing artefacts in pelvic images.

A pelvic image was used to generate k-space data and apply GRAPPA with simulated sensitivity profiles.

Results: The SNR maps at four different slice locations (Fig.2 (a)) of the birdcage coil and the 8-element surface coil array are compared in Fig. 2(b). Although the SNR distribution of the birdcage coil was very homogeneous, the intensity was much lower than that of the surface array. As a result of local sensitivity enhancement, the surface SNR of the coil array was 9 times higher than that of the birdcage coil, whereas the central SNR of the rectangular coil array had about 90% increase compared to the birdcage coil. The parallel imaging ability of the proposed rectangular coil array was evaluated with the GRAPPA algorithm [2], when the reduction factor ranged from 1 to 4. The image size was 128×128 and the number of auto-calibration lines was 24. As indicated with red arrows, minor aliasing artefacts were observed when R = 3, but the cysts/tumours were not affected by these artefacts. However, when R = 4, more aliasing lines started to emerge, which may be of concern for differentiating one of the tumours marked with the red circle.

Conclusion: While the dedicated open body coil had no impact on imaging during irradiation, the proposed radio-transparent surface coil array has the capability to further improve SNR from about 90% to 9-fold from the centre to the surface of the ROI. The coil should be able to achieve an acceleration factor of three without prominent aliasing artefacts.

References:

1. G P Liney et al., *Phys. Med. Biol.* Vol. 45, 135005 (2018).
2. C. M. Collins et al., *Magn Reson Med.* Vol. 45, 692-9 (2001).
3. M. A. Griswold et al., *Magn Reson Med.* Vol. 47, 1202-1210 (2002).

SENSITIVITY BIAS CORRECTION OF A SURFACE COIL ARRAY FOR THE MRI-LINAC SYSTEM

Mingyan Li[1], Ewald Weber[1], Feng Liu[1], Stuart Crozier[1]
[1] School of Information Technology and Electrical Engineering, The University of Queensland

Introduction: Due to the small diameter of spherical volume (DSV) and the reserved windows for radiation beams, the individual coil element of a dedicated 8-element coil array for MRI-LINAC are potentially smaller than those of conventional body array coils, leading to shallower RF penetration and stronger local sensitivity bias. In parallel imaging, the preferred GRAPPA [1] algorithm generally produces less aliasing artefact than other parallel imaging methods, but the combined image with sum-of-square (SOS) method has observable sensitivity bias unless the sensitivity weightings are taken into consideration. In this work, a sensitivity bias correction method based on numerical calculations, SENSE [2] and GRAPPA is proposed for the MRI-LINAC system.

Material and method: Sensitivity bias correction requires sensitivity information, which is normally obtained with extra scans. However, tumour tracking in the MRI-LINAC demands rapid imaging. Since the B_0 strength of MRI-LINAC system is still within the quasi-static regime; with known coil geometry, the receive sensitivity of the coil can be pre-calculated with the Biot-Savart law or with electromagnetic simulation software [3], which will negate the need for extra scans. The coil sensitivity can then be calculated as [4]:

$$B_1^- = \frac{(B_{vx} - iB_{vy})^*}{2}$$

where B_{vx} and B_{vy} denotes the x and y component of the calculated transverse magnetic field from numerical calculations. * denotes conjugate transpose.

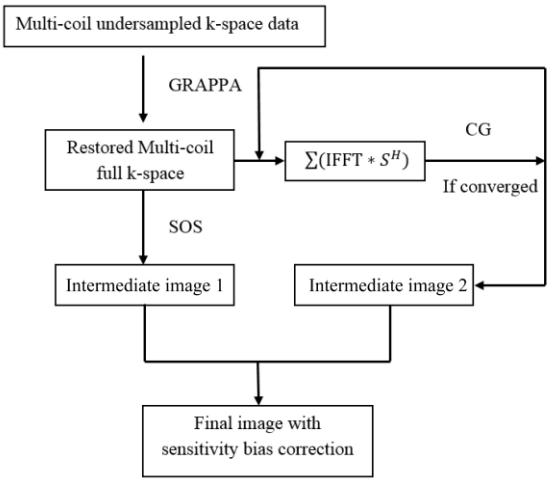

Figure 1 Flow chart of the proposed method for sensitivity bias correction

The proposed method is demonstrated with the flow chart in Figure 1. The undersampled k-space data are firstly reconstructed with GRAPPA and combined to generate an intermediate image 1 with SOS method.

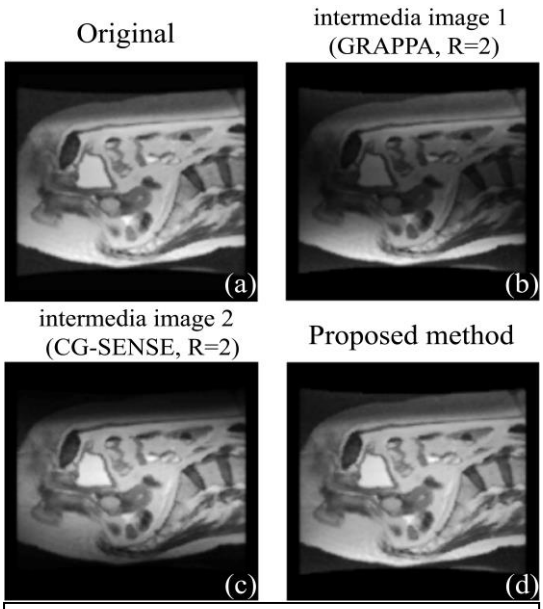

Figure 2 (a) original image (b) Image reconstructed with GRAPPA. (c) Image reconstructed with CG-SENSE. (d) Image reconstructed with the proposed method.

The individual coil images reconstructed from GRAPPA are then multiplied with conjugate transpose of pre-calculated sensitivity profiles. The second intermediate image is restored with a conjugate gradient-SENSE (CG-SENSE) method. The combination of two intermediate images will generate an image without prominent sensitivity bias.

Results: In Fig. 2, the images were reconstructed from GRAPPA (b) and CG-SENSE (c) with half of the k-space data (reduction factor R = 2). As shown in Fig. 2(b), the centre of the image reconstructed with GRAPPA is dark due to the coil sensitivity weighting; whereas the images reconstructed from SENSE (Fig. 2 (c)) have opposite weightings as a result of multiplying conjugate coil sensitivity during restoring the image. By combining the intermediate images produced by GRAPPA and SENSE, the sensitivity bias is successfully removed in the final image (d).

Conclusions: Due to the special geometrical constrains in the MRI-LINAC system, the proposed 8-element coil array has stronger sensitivity bias in the acquired images than would be normal. In this work, a sensitivity bias correction algorithm was proposed to efficiently remove intensity variations caused by local sensitivity weightings. This method is applicable for both fully and subsampled k-space.

References

1. M. A. Griswold et al., *Magn Reson Med.* Vol. 47, 1202-1210 (2002).
2. K. P. Pruessmann et al., *Magn Reson Med.* Vol. 46, 638-651 (2001).
3. J. Jin et al., J Magn Reson. Vol. 207, 59-68, (2010)

GRADIENT NONLINEARITY (GNL) CORRECTION FOR MRI-LINAC SYSTEM

Shanshan Shan[1], Gary Liney[2] , Mingyan Li[1], Fangfang Tang[1], Ewald Weber[1] , Feng Liu[1] , Stuart Crozier[1]
[1] The University of Queensland, s.shan@uq.edu.au
[2] Ingham Institute, Gary.Liney@health.nsw.gov.au

Introduction: MRI-Linac requires precise target delineation of a tumour for accurate radiotherapy treatment [1]. However, the split MRI-Linac gradient structure inevitably produces gradient non-linearity (GNL) manifested as image distortions including geometric deformation and intensity variation [2]. If not resolved properly, these image distortions could degrade the quality of radiotherapy treatment and even lead to unnecessary radiation dose delivered to surrounding healthy tissues [3]. Normally, phantom measurements with fitting models such as spherical harmonic or spline models are used to correct GNL-induced distortions. A potential limitation of these models is that the accuracy may not be guaranteed at the boundary of the field of view (FOV) where the GNL increases strongly. Recently, we proposed a novel hybrid method [4] [5] that combines electromagnetic (EM) modelling and phantom measurement to correct distortions for the MRI-Linac system. Here, experimental results were analysed to validate the proposed method.

Materials and Methods: The distortion correction strategy consisted of two parts, the first of which was the characterisation of the nonlinear gradient field B_{GNL}. This step was realised with the phantom measurement and EM modelling. Here, a grid phantom with specially designed markers was developed in order to calculate the gradient field $B_{markers}$ on these limited maker positions [2]. With the information $B_{markers}$, the current density was estimated through EM modelling. The obtained current density was then used to calculate the nonlinear gradient field B_{GNL}. After that, the second part was to correct image distortions directly with *k*-space domain based method [4].

Figure 1. A prototype phantom measuring an effective volume of 200mm×200mm×300mm

Results: Phantom images before and after GNL correction are shown in Figures 2 and 3, respectively. In the left column, geometric distortions are clearly visible, especially at the outer regions indicated by red arrows. However, after applying the proposed method, these distortions are dramatically reduced as demonstrated by the images in the right columns. After GNL correction, the maximum error of markers in Figure 3 decreased from 8.1 mm (before correction) to less than 2 mm, showing significant improvement in the geometric accuracy.

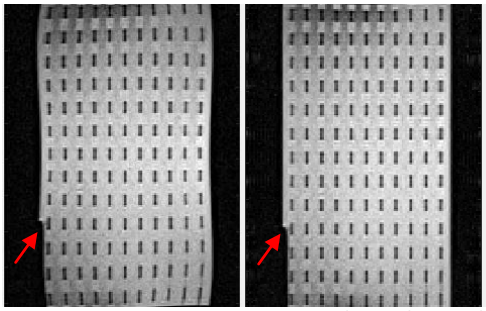

Figure 2. Phantom images at YZ plane before (left) and after (right) distortion correction

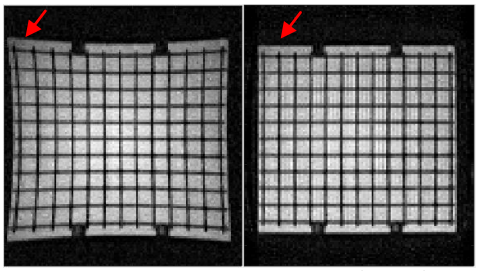

Figure 3. Phantom images at XY plane before (left) and after (right) distortion correction

Conclusion: In this work, a hybrid method combining phantom measurement and EM modelling was developed to correct the GNL for the MRI-Linac system. The experimental results demonstrated that the proposed method can correct GNL-induced image distortions efficiently. In the future, the proposed method will be tested on healthy volunteers.

References:

1. P. J. Keall, M. Barton, and S. Crozier, "The Australian magnetic resonance imaging–linac program." pp. 203-206.
2. D. Wang, D. M. Doddrell, and G. Cowin, "A novel phantom and method for comprehensive 3-dimensional measurement and correction of geometric distortion in magnetic resonance imaging," Magnetic resonance imaging, vol. 22, no. 4, pp. 529-542, 2004.
3. Z. Chen, C. Ma, K. Paskalev, J. Li, J. Yang, T. Richardson, L. Palacio, X. Xu, and L. Chen, "Investigation of MR image distortion for radiotherapy treatment planning of prostate cancer," Physics in Medicine & Biology, vol. 51, no. 6, pp. 1393, 2006.
4. S. Shan *et al.*, "A Novel Hybrid Method for Gradient Nonlinearity (GNL) Correction for MRI-Linac system," in *JOINT ANNUAL MEETING ISMRM-ESMRM*, Paris,France, 2018
5. F. Liu, A. Trakic, H. Sanchez, E. Weber and S. Crozier, Reverse engineering of gradient coil designs based on experimentally measured magnetic fields and approximate knowledge of coil geometry-application in exposure evaluations, *Concepts in Magnetic Resonance*, vol.35B(1), pp.32-43, 2009.

REAL-TIME DELIVERY VERIFICATION FOR MLC TRACKING RADIOTHERAPY USING TIME-RESOLVED EPID IMAGING

Benjamin Zwan[1,2], Vincent Callait[3,4], Jeremey Booth[3,4], John O'Connor[2], Paul Keall[4], Peter Greer[2,5].

[1] Central Coast Cancer Centre, Gosford Hospital, Gosford, NSW. Benjamin.zwan@health.nsw.gov.au
[2] School of Mathematical and Physical Sciences, University of Newcastle, Newcaslte, NSW.
[3] North Sydney Cancer Centre, Royal North Shore Hospital, Sydney, NSW.
[4] Radiation Physics Laboratory, Sydney Medical School, University of Sydney, Sydney, NSW.
[5] Department of Radiation Oncology, Calvary Mater Hospital, Newcastle, NSW.

Introduction: A principal application of MRI-linac devices is to account for intrafraction target motion using real-time adaptive radiotherapy. One method of real-time adaptation is multileaf collimator (MLC) tracking, where the MLC positions are modified in real-time to account for measured 3D target motion. This technique has been implemented on conventional linear accelerators (linacs) to account for prostate motion[1] and respiratory motion of lung tumours using implanted electro-magnetic transponders[2]. MLC tracking is well-suited to implementation on an MRI-linac device due to the availability of target motion from real-time MR imaging. MLC tracking results in more complex MLC trajectories and introduces additional modes of failure into the delivery and this necessitates independent real-time delivery verification. We present a system that relies on time-resolved EPID imaging to verify the MLC in real-time during MLC tracking radiotherapy. This system can be applied for use in both conventional and MRI-linac radiotherapy. This system has been applied retrospectively to MLC-tracking deliveries on a conventional linac with the intention of extending these methods to an MRI-linac system in the future.

Method: Transmission EPID image frames were acquired at 10 frames-per-second during MLC-tracking deliveries as part of the LIGHT SABR trial for lung SBRT patients. During each delivery lung tumour motion was measured using implanted transponders and the Varian Calypso system. For verification, MLC positions were extracted from each EPID image frame[3] and three comparison metrics were used to assess the MLC in real-time: (1) field location, (2) field size and, (3) field shape. As well as analysis of patient data, phantom-based measurments were performed using a 6D Hexamotion stage in order to assess sensitivity and detection delay for a range of MLC delivery errors. During these tests real-time analysis was simulated offline using acquired images and motion from the Calypso system.

Results: For a typical lung tumour tracking delivery, Figure 1 shows an example of the three proposed metrics for real-time verification. For lung test deliveries the MLC-defined field size was measured with an accuracy of 0.3 cm^2 (1 SD). The differences between the field location from the EPID and the target location from Calypso were 0.1±0.3 mm (μ±1SD) in the direction parallel to MLC motion and 0.3±1.5 mm perpendicular. Field location errors (i.e. tracking in wrong direction) with a magnitude of 3 mm were detected within 0.4 s of occurrence in the X direction (parallel) and 0.8 s in the Y direction (perpendicular). Systematic MLC gap errors were detected as small as 3 mm.

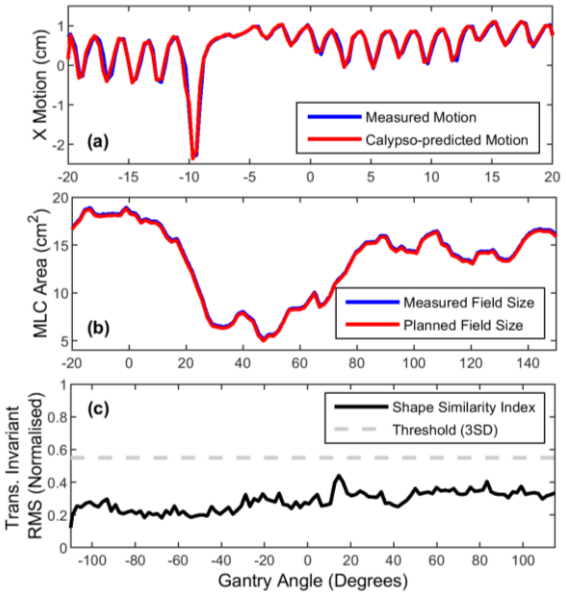

Figure 1. Example of real-time verification of (a) field location, (b) field size and (c) field shape for a lung tracking delivery.

Conclusion: EPID imaging may be used for independent real-time verification of MLC trajectories during MLC tracking deliveries. The EPID-based system has been shown to be sensitive to a range of delivery errors and is applicable to both conventional and MRI-linac devices when MLC tracking is employed.

References:

1. The first clinical implementation of electromagnetic transponder-guided MLC tracking (P.J. Keall et al.) *Med Phys* **41** (2014).
2. The first patient treatment of electromagnetic-guided real-time adaptive radiotherapy using LC tracking for lung SABR (J.T. Booth et al.) *Rad Onc* **121**, 19-25 (2016).
3. An EPID-based system for gantry-resolved MLC quality assurance for VMAT MLC (B.J. Zwan et al.) *JACMP* **17**, 348-365 (2016).

FULLY-AUTOMATIC SEGMENTATION OF MULTIPLE BONE METASTASES FROM LUNG PRIMARY USING FDG-PET/CT IMAGES

R. Nigam[1,2], L. Holloway[1,2,3,4,6,7], M. Carolan[5], M. Fields[2], G. Harris[8], M. Barton[2,3,4], P. Metcalfe[1,2]
[1] Centre for Medical Radiation Physics, University of Wollongong, Wollongong, NSW, 2522, Australia, rn393@uowmail.edu.au
[2] Ingham Institute for Applied Medical Research, Liverpool, NSW, 2170, Australia.
[3] Liverpool and Macarthur Cancer Therapy Centre, Liverpool, NSW 2170.
[4] South Western Sydney Clinical School, University of New South Wales, Liverpool, NSW, 2170, Australia.
[5] Illawarra Cancer Care Centre, Wollongong Hospital, Wollongong, NSW, 2500, Australia.
[6] Institute of Medical Physics, University of Sydney, Camperdown, NSW, 2505, Australia.
[7] Sydney Medical School, University of Sydney, Camperdown, NSW, 2505, Australia.
[8] Chris O'Brien Lifehouse, Camperdown, NSW 2050, Australia.

Introduction: Metastatic non-small cell lung cancer (NSCLC) is the most commonly diagnosed lung cancer and is a leading cause of cancer related mortality[1]. Radiotherapy is a benchmark in the treatment of this disease, given with a palliative intent to provide symptom control and pain relief. Traditionally this disease is considered incurable, but this belief has now been challenged. With the help of improved imaging techniques like PET/CT it is possible to identify patients early in the metastatic spectrum and offer potentially curative local treatments like stereotactic ablative body radiotherapy (SABR)[2]. In order to determine the feasibility of cure or progression free survival of patients with metastastic NSCLC it is crucial to determine the distribution of metastatic disease. Nearly 30-50% of the metastases in NSCLC have bony involvement[1]. However, whole-body detection of multiple metastatic bone lesions on multimodality PET/CT imaging is tedious and error prone. Therefore, aim of this project is to develop a fully automatic software for quantification of the burden of metastatic lung cancer involving bone to estimate the maximum volume of disease for which SABR would be within bone marrow tolerance.

Materials and Methods: This study employed thresholding methods[3] to combine the metabolic information from 18-F-FDG PET that offers high sensitivity in detection of small isolated bone lesions[4], and anatomical information from CT for fully automatic detection, auto-contouring and quantification of whole-body metastatic bone lesions in NSCLC.A total of 10 FDG-PET/CT scans of patients with stage IV were selected. PET/CT scan was performed using GE Discovery 710 scanner. The threshold-based[3] image segmentation algorithm was implemented in MATLAB (Mathworks, Natick, MA) version R2018A. Ouput was visualized using 3D Slicer.

Results: Fig. 1 shows the axial view of a fused PET and CT image. The output of the software shown as color-coded auto-contours for standard uptake value - SUV 2.5, 3, and 3.5. The algorithm used the CT data to built a binary mask of the skeleton. PET intensities were converted into a SUV map. The voxel-wise integration of binary mask and SUV map resulted in systematic elimination of unwanted uptakes such as bladder, liver, kidney, and brain. Finally, SUV thresholding created a binary mask of detected bone lesions, from which auto-contours were created as shown in Fig. 1. The software also performs quantitative analysis on each detected lesion and computes lesion statistics including volume, SUV_{mean}, SUV_{max}, coordinate of hottest voxel in the lesion, standard deviation, total number of lesions detected and total metastatic bone burden. Summary of the quantification of metastatic bone disease is shown in Table 1.

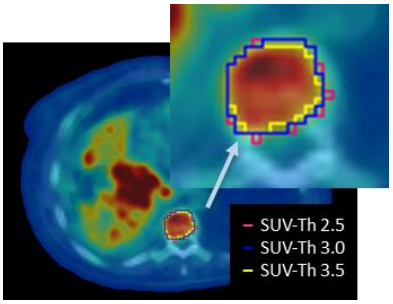

Figure 1. Automatic detection and segmentation of a bone lesion using range of SUV thresholds

Table 1. Distribuation of bone metastasis for range of SUV thresholds computed using cluster analysis

SUV-Th	Number of bone lesions detected	PET Positive Bone Vol (%)	Average SUV_{mean}	Average SUV_{max}	Execution time (sec)
2	67	10.5	2.72	4.61	98.61
2.5	46	6.4	3.41	5.59	60.76
3	33	4.2	4.00	6.25	44.14
3.5	29	3.1	4.57	6.73	34.15
4	23	2.3	5.13	7.29	25.78

Conclusion: A fully-automatic, fast and robust software application has been developed for detection, auto-segmentation and quantification of metastatic bone lesions. Developing similar tools for MRI sequences and MRI-linac applications would be highly beneficial.

References:

1. D. Santini et al. *Nature Scientific Report.***5,** 18670 (2015).
2. A. CTree et al. *Lancet.* **14**, e28-37 (2013).
3. B Foster et al. Comput Biol Med. **50**: 76–96 (2014).
4. GJ O'Sullivan et al. *World J Radiol.* **7(8)**, 202-211 (2015).

DUO SILICON ARRAY DETECTOR PROFILES IN TRANSVERSE AND INLINE STATIC MAGNETIC FIELDS

SJ Alnaghy[1,2], T Causer[1-3], M Gargett[1,4], BM Oborn[1,3], M Petasecca[1], N Roberts[1,2], L Holloway[1,2,5-8], AB Rosenfeld[1], P Metcalfe[1,2]

[1] Centre for Medical Radiation Physics, University of Wollongong, Wollongong, sjh190@uowmail.edu.au
[2] Ingham Institute for Applied Medical Research, Liverpool
[3] Illawarra Cancer Care Centre, Wollongong Hospital, Wollongong
[4] Northern Sydney Cancer Centre, Royal North Shore Hospital, St. Leonards
[5] Department of Medical Physics, Liverpool and Macarthur Cancer Therapy Centres, Liverpool
[6] South Western Sydney Clinical School, University of New South Wales, Liverpool
[7] Institute of Medical Physics, University of Sydney, Camperdown
[8] Sydney Medical School, University of Sydney, Camperdown

Introduction: Magnetic field effects on dose distribution and detector functionality are non-negligible. A permanent magnet named Magnetic Apparatus for RaDiation Oncology Studies (MARDOS) paired with a standard linac offers either transverse or inline orientations of the magnetic field with respect to the radiation beam. MARDOS consists of neodymium-iron-boron magnets with steel cones attached. It provided an ideal preliminary set up for observing magnetic field effects with silicon array detectors before the MRI-linac was available for testing with these detectors.

The detector utilised to investigate these magnetic field effects was DUO silicon detector. The results were compared to previously published MagicPlate-512 (M512) data[1]. DUO has a higher resolution (200 µm) than M512 (2 mm), and hence should be better suited to measuring changes in the dose distribution due to the magnetic field. DUO was also compared to Gafchromic EBT3 film to highlight any intrinsic magnetic field effects in the silicon.

Materials and Methods: Measurements were performed on MARDOS and a Varian 2100C Linac at 6 MV with a dose rate of 600 cGy/min. DUO has 505 sensitive volumes, each volume = 800 × 40 × 100 µm^3, in two orthogonal, linear arrays. DUO was inserted into the magnet cones. The field strength for inline was 0.95 T, and for transverse was 1.2 T. The SSD was 150 cm. Custom phantoms were cut from solid water and solid lung. Profiles were compared between the magnetic fields and 0 T. Small field sizes were investigated, which were also constrained by the magnet cones. DUO was then replaced with film in the same set-up. The size of the air gap above the sensitive volumes of DUO needed to be investigated in the transverse orientation due to the anticipated magnetic field effects. FWHM, 80-20% penumbral widths and maximum dose differences between detectors and between the presence/absence of a magnetic field were investigated. Symmetry was determined to be an appropriate additional metric to investigate profile skewness under the transverse magnetic field.

Results: The static inline magnetic field had minimal effect on the profiles in solid water. As expected, the lower density of solid lung meant that this material was more susceptible to generating magnetic field effects in the dose deposited. The greatest penumbral narrowing due to the inline field (0.7 mm) occurred in lung, however these differences were within the ±1 mm positional tolerance of the jaws[2]. All three detectors agreed to within this tolerance. Dose enhancement was greatest in lung (maximum: 9%). The transverse field distorted the profiles in the direction of the magnetic force. The penumbra were widened, most notably in the solid lung phantom, by a maximum of 2.3 mm. The largest asymmetry due to the transverse field (4.6%) was also in solid lung. Average uncertainties were within ±2.7% for DUO, ±3.1% for film and ±3% for M512[1].

Conclusions: The extrinsic magnetic field effects on dose were measured with DUO detector and the intrinsic effects were observed by comparing to film. DUO was found to be an appropriate alternative to M512, with improvement in terms of its higher resolution. MARDOS provided a suitable environment for these preliminary tests. Measurements with these detectors on the MRI-linac are now in the early stages.

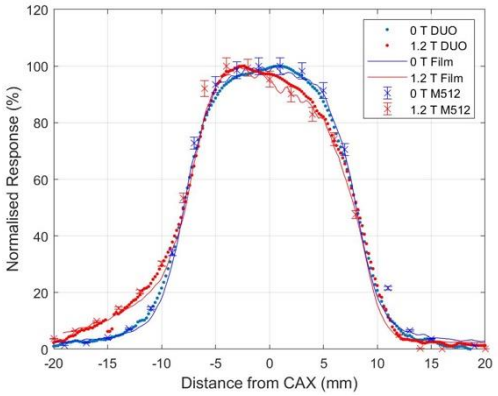

Figure 1. Solid lung profiles in a transverse magnetic field

References:

1. A high resolution 2D array detector system for small-field MRI-linac applications (M Gargett et al.), *Biomed. Phys. Eng. Express* **4**(3), 1-11 (2018).

LINAC PHOTON BEAM DOSIMETRY USING A PLASTIC SCINTILLATION DOSIMETER AND A CONVOLUTIONAL NEURAL NETWORK

Levi Madden[1], James Archer[1], Enbang Li[1], Dean Wilkinson[2], Anatoly Rosenfeld[1,3]
[1] University of Wollongong, NSW 2522, Australia email:ljm898@uowmail.edu.au
[2] Illawarra Cancer Care Centre, Wollongong, NSW 2522, Australia.
[3] Illawarra Medical and Health Research Institute, University of Wollongong, NSW 2521, Australia.

Introduction: Plastic scintillation dosimeters (PSDs) possess many desirable qualities that make them promising for relative dosimetry [1]. The dose deposited in a scintillators volume is proportional to the number of photons emitted by the scintillator. A PSDs response is less dependent on magnetic field strength than an ionisation chamber when measuring the dose in MR-LINAC fields [2], while the PSD remains more water equivalent.

The LINAC irradiation of a plastic scintillation dosimeter results in the production of scintillation and Cerenkov radiation optical signals [1]. A method must be employed to measure the scintillation present in the combined scintillation and Cerenkov radiation (total) optical signal [1]. In recent work, artificial and convolutional neural networks have been applied to measure the scintillation signal present in a temporal waveform of an input combined scintillation and Cerenkov radiation waveform [3,4].

Materials and Methods: The PSD was comprised of a plastic scintillator volume (Saint Gobain BC444) optically coupled to a plastic optical fiber (Eska CK40). The scintillator was cylindrical with a length 0.5 mm and a diameter of 2 mm, while the optical fiber had an inner core diameter of 1 mm. The scintillator volume was coated with diffusive reflective paint (Saint Gobain BC620) to improve the scintillation collection efficiency of the optical fiber.

A photomultiplier tube (RCA 4526) and digital oscilloscope (Picoscope PS6404) was used to measure the total optical signal as a function of time. A Varian 21iX Clinac was irradiated the PSD with a 6 MV photon beam at a dose rate of 600 MU/min. Solid water (Gammex RMI 457) was used as the phantom material for the collection of beam profiles. Beam profiles were collected at a depth of 1.5 cm, a source to surface distance of 100 cm and field sizes of 3 cm by 3 cm, 5 cm by 5 cm and 10 cm by 10 cm.

The convolutional neural networks (CNNs) were trained following the procedure outlined in Madden et al [4]. The CNNs measure of the Cerenkov radiation signal was subtracted from the input combined signal; the difference in these was integrated to determine the scintillator measured dose. The CNNs measure of dose was compared to the dose measured by an ionisation chamber (Scanditronix CC13) and the known scintillator dose as measured using the gold standard method for Cerenkov radiation measurement, background subtraction [1].

Results: The measured dose profiles are plotted in Fig 1. Mean absolute differences in dose were calculated between the CNN and ionisation chamber doses (CNN-IC discrepancy) and the background subtraction and ionisation chamber doses (BS-IC discrepancy). The mean absolute difference in dose were on average 1.4% for the CNN-IC discrepancy, matching the 1.4% BS-IC discrepancy.

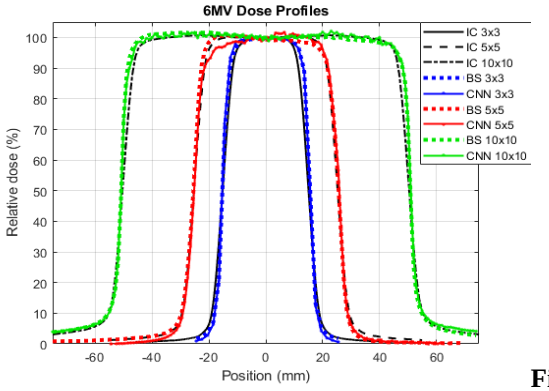

Figure 1: Measured dose profiles. IC, BS and CNN are the ionisation chamber, background subtraction and CNN measured dose profiles, respectively. 3x3, 5x5 and 10x10 are the dose profiles measured at the 3 cm by 3 cm, 5 cm by 5 cm and 10 cm by 10 cm field sizes, respectively.

Conclusions: The CNN method applied for dose measurement had an accuracy matching that of background subtraction when comparing each method with an ionisation chamber. The time required for a CNN to process an input waveform was on average 3 ms, making the CNN PSD dosimetry method applicable for real time dosimetry. The ability for PSDs to remain unaffected by strong MR fields makes their application as MR-LINAC dosimeters promising.

References:

1. Review of plastic and liquid scintillation dosimetry for photon, electron, and proton therapy (L. Beaulieu et al.) *Phys. Med. Biol.* **61**, R305-43 (2016).
2. Effect of magnetic field strength on plastic scintillation dosimeter response (F. Therriault-Proulx et al.) *Rad. Meas.* **10**, 10-13 (2018).
3. Temporal separation of Cerenkov radiation and scintillation using artificial neural networks in Clinical LINACs (L. Madden et al.) *Phys. Medica.* **54**, 131-136 (2018).
4. Temporal separation of Cerenkov radiation and scintillation using a clinical LINAC and artificial intelligence (L. Madden et al.) *Phys. Med. Biol.* in press (2018).

FIRST EXPERIENCES WITH HEALTHY VOLUNTEER ROTATION FOR MRI-GUIDED RADIOTHERAPY: THE PAROT STUDY

Jarryd Buckley[1,2], Gary Liney[1,2,,3], Jason Dowling[1,4], Robba Rai[2,3], Lois Holloway[1,2,3], Peter Metcalfe[1,2], Paul Keall[2,5]

[1] Centre for Medical Radiation Physics, University of Wollongong, NSW, Australia, jgb552@uowmail.edu.au
[2] Ingham Institute for Applied Medical Research, Liverpool, NSW, Australia
[3] Liverpool Hospital Cancer Therapy Centre, South West Sydney Local Health District, NSW, Australia
[4] CSIRO Australian eHealth Research Centre, Herston, QLD, Australia
[5] ACRF Image-X Institute, School of Medicine, University of Sydney, Sydney, NSW, Australia

Introduction: The Australian MRI-Linac comprises of a 6 MV Linear Accelerator (LINAC) (Varex, Linatron) coupled with a bespoke split-bore 1 Tesla superconducting magnet (Agilent, UK) shown in Figure 1(a)[1]. The system is unique in that the LINAC position/gantry angle is fixed.

Figure 1: (a) The Australian MRI-Linac system. (b) The patient rotation system on the departments dedicated 3 Tesla clinical MRI scanner.

Therefore, to recreate multiple treatment beam angles, horizontal rotation of the patient is required. No literature exists on the tolerability of horizontal rotation within an MRI scanner, and little on the effects of rotation on internal organ deformation. A local HREC approved study (PAROT) has therefore been initiated at our centre to investigate the above. We present initial results on a cohort of 10 healthy volunteers.

Method: Psychometrically validated questionnaires assessing claustrophobia (CLQ)[2], anxiety (STAI)[3] and motion sickness (FMS)[4] were completed prior to imaging. Volunteers were imaged on a patient rotation system[5] with a 5 minute high quality T2 turbo spin echo (TSE) isotropic scan (SPACE) and at 45° intervals through a full 360° with a 55 second 2D TSE scan(Figure 1 (b)) on a 3 Tesla dedicated radiotherapy scanner (Siemens Skyra). The anxiety and motion sickess questionnaires were re-administered following the imaging to assess any change using a Wilcoxon sign-rank test, and compared to the volunteers respective baseline clastrophobia score.

Internal deformation of soft tissue was assessed by first rotaing each image back to the 0° position, then applying a rigid[6] and non-rigid[7] registration of each angled image to the 0° scan as shown in (Figure 2).

Results: No statistically significant change in anxiety (p=0.195) or motion sickness (p=0.125) was observed. No correlation was apparent between anxiety or motion sickness and baseline claustrophobia. Deformations greater than 40 mm were observed around the external surface with much smaller deformation in the central anatomy.

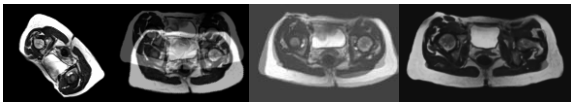

Figure 2: Image registration workflow (L-R) angled MRI image, image rotated back to 0°, rotated image rigidly registered to 0° image, non-rigid registration to the 0° image.

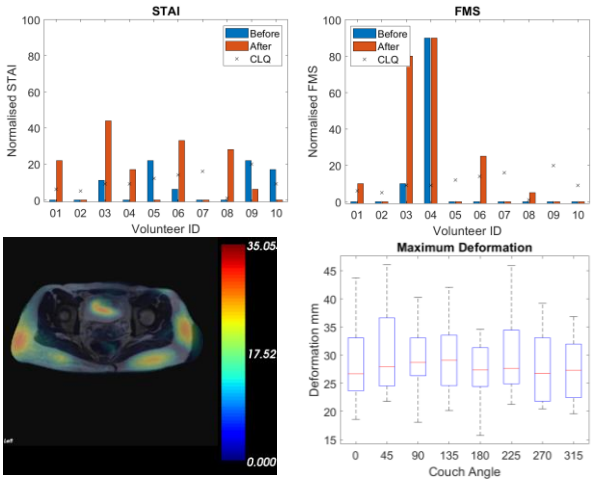

Figure 3: (a) anxiety and (b) motion sickness before and after imaging (c) deformation field of volunteer 09 135° scan registered to 0° (mm) and (d) boxplot of maximum deformations for each couch angle.

Conclusion: No significant change in anxiety or motion sickness was observed for volunteers undergoing rotation within an MRI scanner. Deformation was greatest close to the external surface but was reduced in the central anatomy. Based on these results, MRI-guided radiotherapy with a fixed beam may be feasible.

References:

1. Keall PJ et. al. *Semin Radiat Oncol.* 2014;24(3):203-206.
2. Radomsky AS et. al. *Journal of Anxiety Disorders.* 2001;15(4):287-297.
3. Marteau TM et. al. *British Journal of Clinical Psychology.* 1992;31(3):301-306.
4. Keshavarz B et. al. *Hum Factors.* 2011;53(4):415-426.
5. Whelan B et. al. *Medical physics.* 2017;44(2):581-588.
6. Rivest-Hénault et. al. *Medical image analysis.* 2015;23(1):56-69.
7. Vercauteren T et. al. *NeuroImage.* 2009;45(1):S61-S72.

IMAGING RESPIRATORY INDUCED TUMOUR MOTION USING 4D-MRI FOR LUNG CANCERS

Danny Lee[1], Jonathan.Goodwin[2], Kate Skehan[2], Joanne Ludbrook,[2] John Simpson[2] and Peter Greer[1,2]
[1] The University of Newcastle, danny.lee@newcastle.edu.au, [2] Calvary Mater Newcastle, Newcastle, NSW

Introduction: Respiratory-correlated 4D-MRI[1] has gained great interest as an alternative to 4D-CT to quntify respiratory-induced motion throughout the thorax and abdomen, and improve soft-tissue delineation. This study evaluated a self-gated 4D-MRI technique using a 4D motion phantom to quantify tumour motion for lung cancer radiotherapy.

Materials and Methods: A self-gated 4D-MRI technique was utilised to scan a 4D motion phantom (QUASAR™, Modus) which simulates lung tumour motions. A 30.0 mm diameter tumour filled with oil was subject to sinusoidal motion in the superior-inferior (SI) direction with a 30.0 mm amplitude and 4 second period. Additionally a measured patient lung tumour motion with 24.4±2.4 mm measured amplitude from a previous study[2] was scanned.

Reference images were also acquired using 2D cine-MRI (T2 HASTE) and 3D free-breathing (or contrast-enhanced) body imaging (T1-weighted StarVIBE). Quantitative analysis was performed to evaluate tumour motion range.

Results: Two tumour motions shown in Figure 1 were produced during MRI scans.

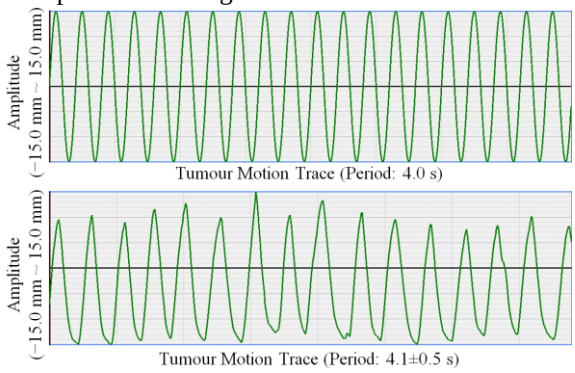

Figure 1. Tumour motions used during MRI scans. A sine wave (top) and lung tumour motion (bottom)

Figure 2 shows images of a static tumour and tumour + motion (tumour motion range). The diameter of the tumours without motion was measured at around 30.0 mm in all MR images. The SI tumour envelope with the simple sine wave motion was measured at 58.2 mm (StarVIBE) and 60.5 mm (Cine and 4D-MRI). In the case of the patient motion pattern, the envelope measured at 48.7 mm (StarVIBE), 58.3 mm (Cine-MRI) and 52.3 mm (4D-MRI).

Table 1. Motion range with/without tumour motion.

Motion Type	Cine-MRI (mm)		StarViBE (mm)		4D-MRI (mm)	
	Static	Motion	Static	Motion	Static	Motion
Sine wave	29.7	60.5	29.7	58.2	30.9	60.5
Tumour	29.7	58.3	29.7	48.7	30.9	52.3

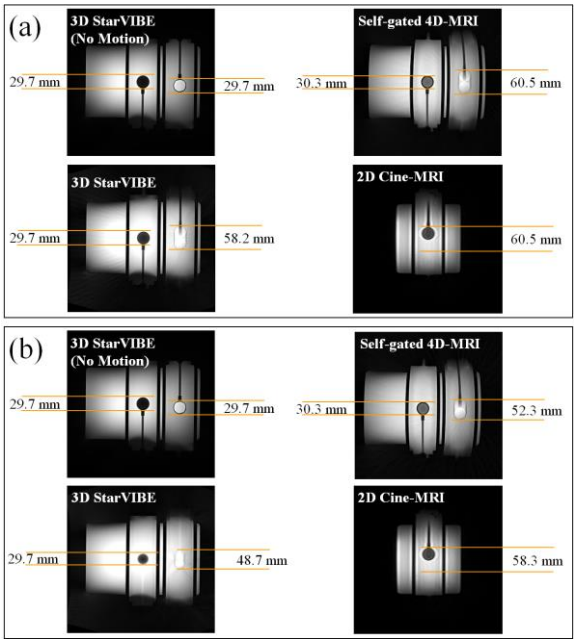

Figure 2. Tumour motion range measured on 3D StarVIBE with/without motion. Self-gated 4D-MRI and 2D Cine-MRI. Produced (a) a sine wave and (b) lung tumour motion during MRI scans.

Cine-MRI produced a similar tumour motion range for both motion patterns reflecting its reduced dependency on motion regularity compared to both StarVIBE and 4D-MRI. A fuller investigation of the accuracy of 4D-MRI incorporating 5 healthy volunteers and 15 lung cancer patients is commencing at the Calvary Mater Newcastle Hospital in early 2019.

Conclusions: This self-gated 4D-MRI techinque is available for lung cancer radiotherapy planning but requires further investigation to characterise its performance under conditions of real patient motion.

Acknowlegdements: We thank Department of Radiation Oncology of Calvary Mater Newcastle and for MRI funding and the Australian MRI-Linac program.

References:

1. Nuts and bolts of 4D-MRI for radiotherapy (B. Stemkens et al.), *Phys. Med. Biol.* **63,** 21TR01 (2018).
2. Audiovisual biofeedback improves cine–MRI measured lung tumor motion consistency (D. Lee et al.) *International Journal of Radiation Oncology* Biology* Physics* **94,** 628-636 (2016).

DISTORTION STUDIES ON A 3T MRI: QUANTIFICATION OF LUNG TUMOUR SUSCEPTIBILITY

Madeline Carr[1,2], L.Holloway[1-3], A. Walker[2,3], P. Metcalfe[1,2]
[1] Centre for Medical Radiation Physics, University of Wollongong, mec640@uowmail.edu.au
[2] Ingham Institute for Applied Medical Research, Liverpool
[3] Department of Medical Physics, Liverpool and Macarthur Hospital Cancer Therapy Centres

Introduction: Magnetic Resonance Imaging (MRI) is progressively becoming utilised in radiotherapy treatment planning (RTP). This is due to its advanced soft tissue contrasting capabilities, allowing for high precision tumour delineation while removing additional dose delivery to a patient [1, 2]. While there are several distortion causing factors that can occur during MR-acquisition, in the lungs additional factors make volume definitions difficult. This includes low-density lung tissue reducing the possible signal-to-noise ratio (SNR) and having a large air-tissue interface. The latter effect induces distortions due to the significant differences in magnetic susceptibility properties that exist between the air and tissue. Such an effect limits the geometrical accuracy of the patient anatomy derived from the scan information, which can be detrimental for applications into MR-only RTP.

In this investigation, a developed susceptibility quantification method was used to determine the extent of such distortions of tumours located within lung-simulated anatomy. Such a method utilised a MATLAB script to quantify these effects occurring during a specific pulse sequence: double-gradient-echo field-mapping sequence, performed using the 3T Siemens MR-Sim Magnetron Skyra located at Liverpool Hospital.

Materials and Methods: A lung phantom was composed, incorporating two distinct air cavities and hence air-tissue interfaces. Several tumours were also created, which were positioned identically within these cavities. Such tumours had the same base glycerine-water solid mixture as the tissue composition, however they were made homogeneously (bolus-like), and inhomogenously (distinct air-gaps between tumorous tissue). The tumour containing phantom was positioned at isocentre within the scanner, and the same pulse sequence was performed and repeated several times for each set-up. This sequence produced two magnitude images from the individual echoes, which varied in phase due to susceptibility-only distortions in the image (after removing associated B_0 inhomogeneity and motion effects). Phase differences were compared on a pixel-by-pixel basis and were output in a corresponding phase image. The greyscale intensities were able to be converted to frequency shifts and mm-sized distortions occurring within a pixel. Ideal imaging parameters found and utilised included a receiver bandwidth (BW) of 875Hz/pixel and difference in echo time (ΔTE) of 1ms.

Results: The inhomogeneous tumour generated the largest pixel distortions within in the image. This had a maximum magnitude of 1.75 ± 0.01 mm, 0.5 mm greater than that for the homogeneous composed tumour.

When the tumours were removed, the largest distortions found were located along the main air-tissue interface of the lung. This was repeated for several BW's with consistent trends found, as seen in Figure 1. For the 875H/pixel BW, as used in the previous investigation, maximum distortions found included a magnitude of 0.47 ± 0.01 mm. As distance from the interface was increased, the size of this distortion reduced by -0.020 mm, per millimetre increase from the interface.

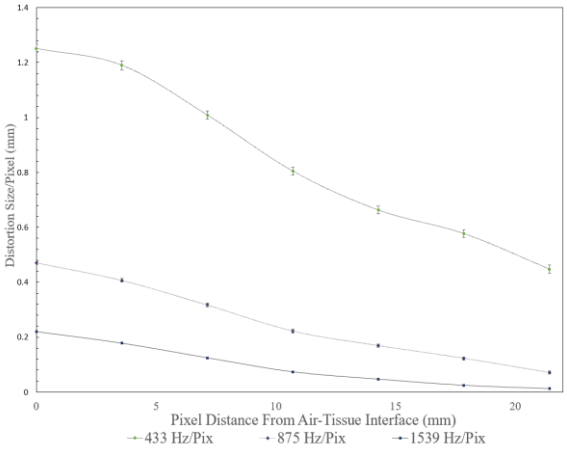

Figure 1. Distortion reductions as distance from the interface was increased, using a variety of BW's.

Conclusions: Tumours with inhomogeneous compositions in the lung (or metastasise in other regions with air quantities present) generated significant (> 0.5 mm) susceptibility distortions in an MR-acquisition. By increasing the distance from the main air-tissue interface of the lung, it reduced the observed distortions also. Regions generating large distortions will require a greater uncertainty for both tumour and normal tissue volume definitions within when using MRI. Incorporating such geometric uncertainties in volume definitions is considered essential for applications into MR-only RTP.

References:

1. A. Fransson et al., Aspects of MR Image Distortions in RTP, *Strahlenther Onkol*, **177**, 59-73 (2001).
2. Collaboration of radiographers and radiation therapists (R. Rai et al.), *Med. Rad. Sciences*, V **64**, 61-68 (2017).